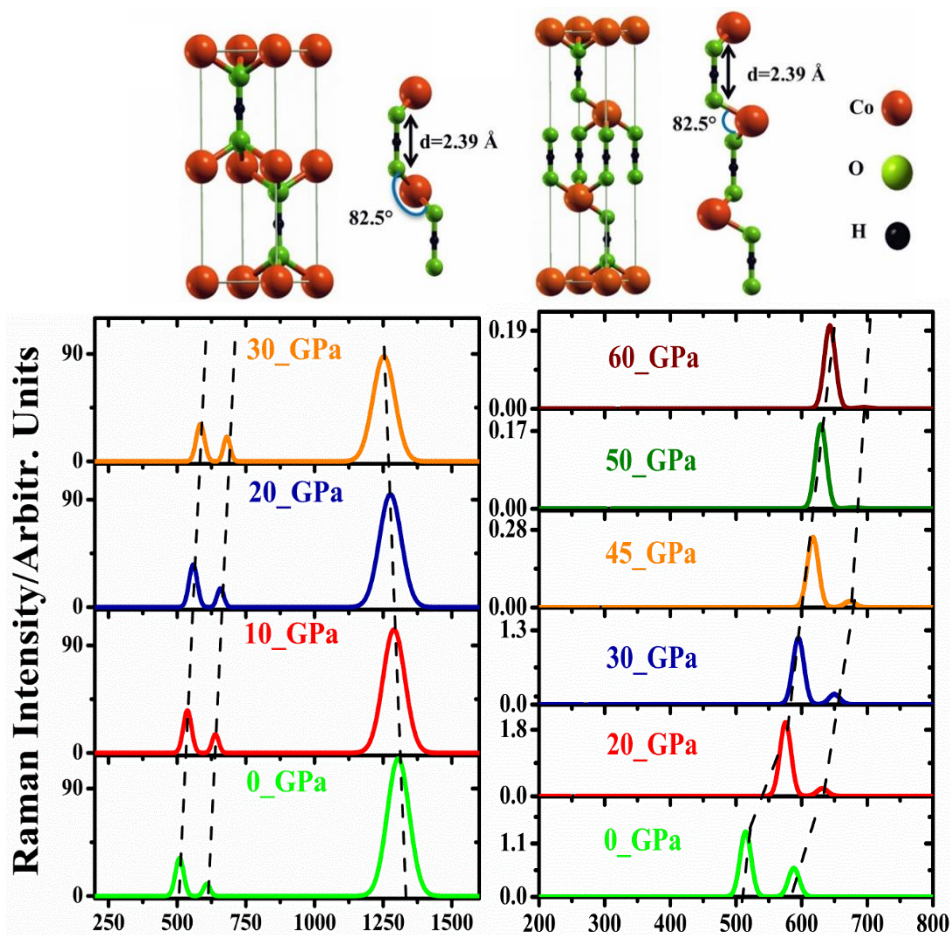


CHAPTER 3

Structural, Electronics, Dynamical and Mechanical Properties of HCoO₂



D. Upadhyay, A. Pratap, P. K. Jha, *J. Raman Spectrosc.* 50, 603-613 (2019)

3.1 Introduction

ABO_2 delafossite-type oxides which exhibit layered structure with p-type conductivity attracted great interest due to their potential uses in optoelectronic, electronic, photovoltaics, rechargeable battery electrodes, catalysis, and electrochemistry [1-9]. They are characterized by the edge-sharing BO_2 octahedra that are stacked along the c axis. The stacking of BO_2 octahedra occurs in two different ways along the c direction, which makes them crystallize in hexagonal 2H (space group $\text{P6}_3/\text{mmc}$) or rhombohedral 3R (space group $\text{R}\bar{3}\text{m}$) crystal symmetries [10]. The numerous properties of both polytypes of delafossite oxides suggest a good structure-property relation in the area of delafossites. Recently, Burlet et al. [13] performed the spectroscopic measurements and proposed a new delafossite structure of cobalt oxy-hydroxides (HCoO_2). The heterogenite HCoO_2 , a hydrogen bonded layered structure of cobalt which exists in the metastable phase [14]. The heterogenite like other ABO_2 delafossites exhibits in two phases; heterogenite-3R in rhombohedral structure with space group $\text{R}\bar{3}\text{m}$ and heterogenite-2H with space group $\text{P6}_3/\text{mmc}$ [15] where the most common form being the 3R-heterogenite phase. To date, only a few attempts have been made to synthesize the HCoO_2 [16, 17]. The relative stability of crystalline cobalt oxides (CoO_2), hydroxides ($\text{CoO}(\text{OH})$), and oxy-hydroxides (CoOOH) in the electrochemical environment is previously reported and indicates that CoOOH and CoO_2 are thermodynamically stable in an oxidizing environment. It is noteworthy that the cobalt oxide electrodes are highly active for oxygen evolution reactions (OER). Additionally, the suspension of ultrathin β - CoOOH nanosheet was used as an efficient photocatalytic hydrogen evolution under visible light and found its use as two-dimensional oxy-hydroxide based photocatalyst for hydrogen production [17]. Present work describes the pressure dependent structural, electronic, vibrational and elastic properties of bulk 2H- and 3R- HCoO_2 using first-principles calculations based on density functional theory. We mainly focus

on the structural features, such as dynamical and mechanical stabilities to understand the structure-property relation of 3R and 2H-HCoO₂ under pressure. Here, we also present a detailed analysis of the phonon mode compatibility of both polytypes of HCoO₂ at symmetry points and directions of Brillouin Zone (BZ) using group theory.

3.2 Computational Methods

All calculations for the HCoO₂ compound were performed using a plane wave pseudopotential method implemented in Quantum Espresso code [19]. The local density approximation (LDA) and generalized gradient approximation (GGA) were used for exchange correlation functional [20–21] in which the energy was parameterized by Perdew, Zunger (PZ) for LDA and Perdew, Burke, and Ernzerhof (PBE) for GGA within norm-conserving pseudopotentials. The electron scalar non-relativistic LDA and scalar relativistic GGA pseudopotentials were used to perform the calculations. Additionally, the on-site Coulomb repulsion U term with LDA functional is used for accurate prediction of band gap [22]. The energy cut-off values for the wave function and charge densities were 100 Ry and 400 Ry respectively. For integral calculations in reciprocal lattice space, we used 10x10x10 k-point grids in the Monkhorst-pack scheme [23]. Geometric optimization was performed by constant pressure variable cell using the Parrinello-Rahman method [24]. The energy convergence value between two consecutive steps was 10^{-4} eV and the maximum Hellmann-Feynman force acting on each atom was less than 0.001 eV/Å. The electron-ion parameters of a unit cell were relaxed under Broyden-Fletcher-Goldfarb-Shannon (BFGS) algorithm [25]. It has ensured that the cell parameters and atomic coordinates both are optimized at each pressure [26, 27]. The calculations of vibrational properties were performed by employing the density functional perturbation theory (DFPT) [28]. The stress has been calculated from thirteen sets of deformed structure, the internal degrees of freedom were again optimized and have been used to calculate

the second order elastic constants, maximum Lagrangian strain 0.15 was used to generate the deformed structure.

3.3 Results and Discussion

3.3.1 Structural Properties

It is well known that the heterogenite HCoO₂ exists either in the hexagonal symmetry with the space group P6₃/mmc or in the rhombohedral symmetry with R $\bar{3}$ m space group. The structural symmetry of this oxide depends upon the stacking sequences of O-Co octahedron layers. The structural geometry of HCoO₂ in hexagonal (2H) and rhombohedral (3R) symmetries are displayed in Fig. 3.1. It can be seen from Fig. 3.1(a) that the hexagonal unit cell possesses two stacking units and these units are periodically repeated. However, for the rhombohedral unit cell (Fig. 3.1(b)) the lower two stacking units are similar to the hexagonal unit cell while the top units have a different stacking sequence than the hexagonal unit cell.

Table 3.1: Calculated lattice parameters of 2H- and 3R- HCoO₂ along with reported experimental (Exp.) and theoretical data

3R-HCoO ₂	LDA	GGA	LDA+U	Exp.	Other theoretical
a (Å)	2.844	2.933	2.843	2.855 ^[13]	-
c (Å)	12.825	13.080	12.854	13.157 ^[13]	-
E_g (eV)	1.17	1.84	2.06	2.0 ^[17] , 1.7 ^[14]	2.16 ^[16]
2H-HCoO ₂	LDA	GGA	LDA+U	Exp.	Other theoretical
a (Å)	2.844	2.933	3.030	2.855 ^[15]	-
c (Å)	8.551	8.723	8.878	8.805 ^[15]	-
E_g (eV)	1.13	1.85	2.01	-	-

The calculated lattice parameters are summarized in Table 3.1 which shows an excellent agreement between available experimental and theoretical data [13, 14, 16]. Further, the ab-initio calculations are carried out up to the pressure of 40 GPa for 2H phase and up to 60

GPa for 3R phase of HCoO_2 enforcing the zero pressure symmetry throughout the simulation. In this pressure range, we have analyzed the structural parameters such as lattice parameters, unit cell volume (v), and O-H distance of both phases of HCoO_2 .

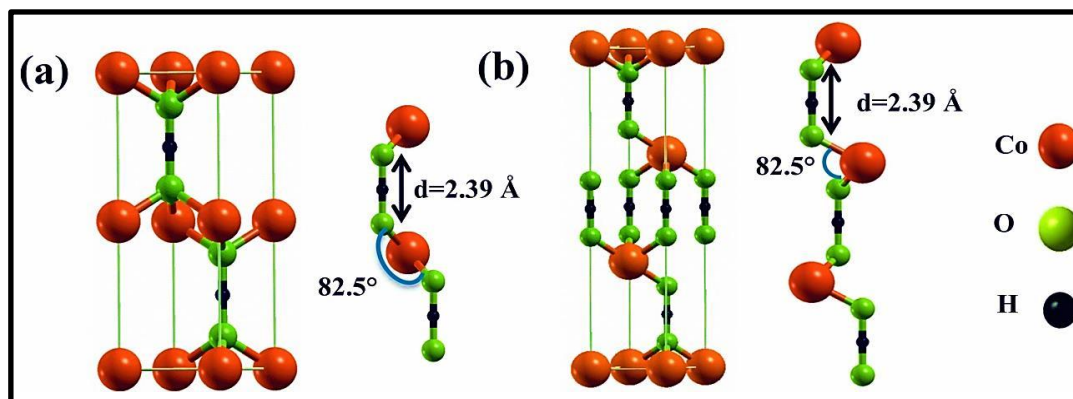


Figure 3.1: Crystal structure of (a) Hexagonal (2H) and (b) Rhombohedral (3R) HCoO_2 .

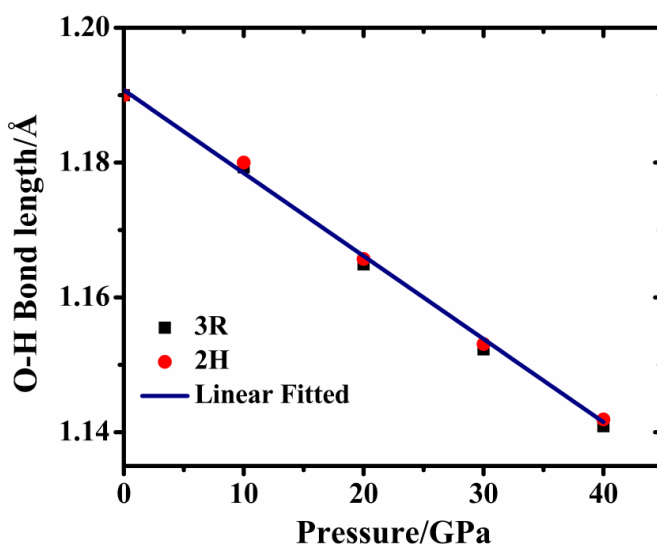


Figure 3.2: Pressure dependent O-H bond length for 2H and 3R- HCoO_2 . Blue line shows the linear fitted curve: $y = (1.19 \pm 0.00008) - (0.00123 \pm 0.000003) x$.

The pressure-dependent O-H bond profile is displayed in Fig. 3.2, which indicates a constant decrease in O-H distance with increasing pressure. The reduced lattice parameters of 2H and 3R- HCoO_2 shown in Fig. 3.3(a-b) indicate that the ratio of c/c_0 and a/a_0 decreases linearly with pressure. It can be seen from Figs. 3.3 (a-b) that 'a' axis is more compressible than 'c'

axis as c/c_0 ratio decreases slowly with pressure as compared to a/a_0 . The O-H bonding becomes very strong with pressure and results in a less compressible structure in z directions.

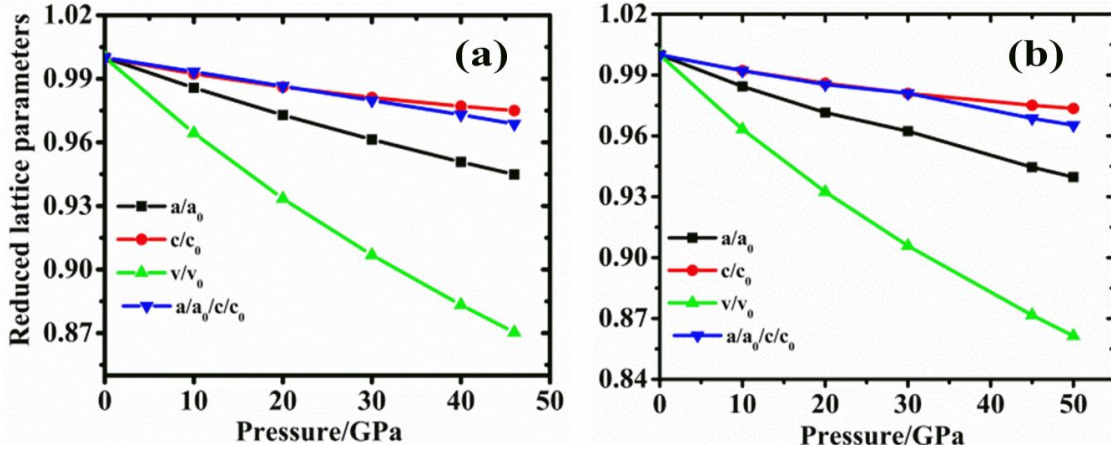


Figure 3.3: Reduced lattice parameters (a , c) and reduced volume (v) as a function of pressure of (a) 2H-HCoO₂ and (b) 3R-HCoO₂. a_0 , c_0 and v_0 are the lattice parameters and volume at 0 GPa.

3.3.2 Electronic Band Structure

The inherent electronic properties and the qualitative analysis of the effective mass of carriers can be easily done by the electronic band structure. Therefore, we have calculated the band structure of 2H and 3R phase of HCoO₂ and is presented them in Fig. 3.4(a) and (b) respectively. The band gap is calculated using LDA, GGA and LDA+U and found in the range of 1.13 eV to 2.06 eV for both the phases of HCoO₂. The only difference in 2H and 3R HCoO₂ is the stacking sequences, however, the similar bonding nature results in similar electronic properties. The calculated electronic band gap of 2.01 eV (2H) and 2.06 eV (3R) using LDA+U show a good agreement with the available experimental value of 2.0 eV [17] for 3R phase. It is also noted that there is no experimentally reported band gap for 2H phase. We have used $U=3.0$ eV for valence Co-d bands, which is consistent with previously reported values [16]. The electronic band structures are calculated along with the high symmetry directions of the Brillouin zone (BZ) i.e. Γ -M-K- Γ and Γ -F-L-Z- Γ for 2H and 3R-HCoO₂ respectively. The band structures calculated using LDA+U show an indirect band gap of 2.01 eV and 2.06

eV for 2H and 3R phases respectively confirming the semiconducting nature of HCoO₂ in both phases.

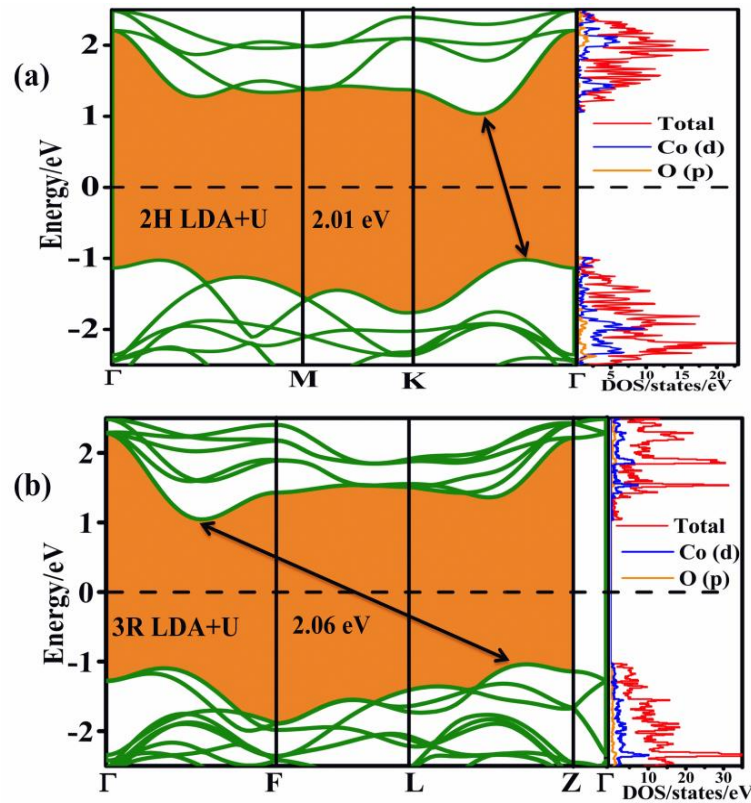


Figure 3.4: The electronic band structure and density of states (DOS) calculated by LDA+U for (a) 2H-HCoO₂ (b) 3R-HCoO₂. The Fermi energy is set to zero.

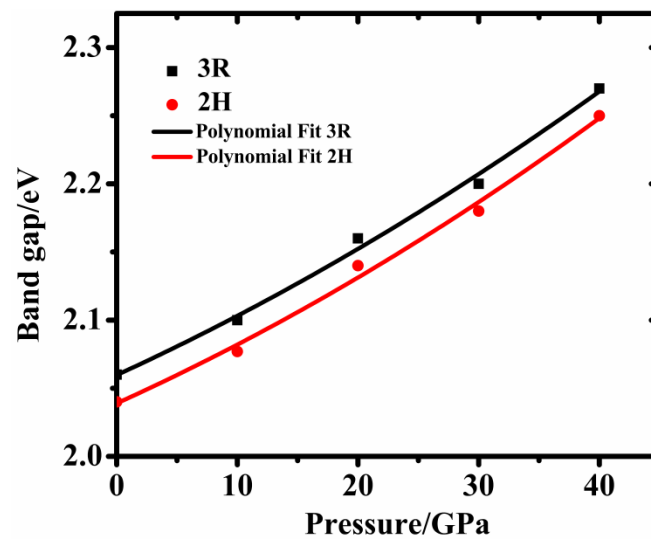


Figure 3.5: Pressure dependent electronic band gap of 2H- and 3R-HCoO₂. Red dots and black squares indicate our calculated value and the corresponding lines show the polynomial fitted curve with equation: $y = 2.012 + 0.00632x - (1.21 \times 10^{-5})x^2$.

Further, the total and partial density of states (DOS) is calculated and presented in the right panel of Fig. 3.4(a) and (b). These figures depict that the d-orbital of cobalt contributes majorly to density of states for both phases. The valence band maximum (VBM) is mainly constructed by the d-orbitals of cobalt and p-orbitals of O atoms. At high pressure, the VBM edge shifts towards the lower energy due to the decrement in volume. As VBM is dominated by Co-d and O-p orbitals, the downshift of the Co-d states reduces the hybridization of the uppermost valence band states leading to an increase in the band gap. This effect is also found in other delafossite type semiconductors [29, 30, 31]. However, in other oxide semiconductors such as the perovskite, the similar effect of hybridization is absent [32]. The pressure variation of the energy band gap of both 2H- and 3R- HCoO_2 is presented in Fig. 3.5. The band gap linearly increases with increasing pressure. It is shown from Fig.3.5 that the pressure increases the band gap of 2H and 3R- HCoO_2 .

3.3.3 Vibrational Properties

A. Phonons

To have an idea about the behavior of phonons and their role played in the stability and possible phase transformation of 2H and 3R phases of HCoO_2 , we have calculated the full phonon dispersion curves (PDC) and Raman spectra at zero and high pressures. The phonon calculations in the present study are performed only using LDA functional. The phonon wavenumbers obtained using LDA functionals give a reasonable description of structural and vibrational properties [28]. For 2H- HCoO_2 and 3R- HCoO_2 , there are 8 and 12 atoms respectively in the unit cell which result in the 24 and 36 phonon branches with 3 acoustic and rest being optical branches. The group theoretical analysis of their space groups ($P6_3/mmc$ and $R\bar{3}m$), depicts the optical modes at the zone center which belongs to the following irreducible representations [33, 34, 35]

$$\Gamma_{optic} = A_{1g} + 3A_{2u} + 2B_{1g} + 2B_{2u} + 2E_{2u} + 2E_{2g} + 3E_{1u} + E_{1g} \quad (3.1)$$

$$\Gamma_{optic} = A_{1g} + 3A_{2u} + 3E_u + E_g \quad (3.2)$$

where symbols g, u, and E respectively represent Raman active, infrared (IR) active, and degenerated modes. The zero pressure PDC of 2H phase along the major symmetry directions of the Brillouin zone (BZ) and the corresponding phonon density of states are shown in Fig. 3.6(a). The phonon density of states is important to calculate the lattice specific heat and several other thermodynamical functions [36, 37]. It can be seen from Fig. 3.6(a) that there does not exist any phonon mode with imaginary frequency confirming the dynamical stability of this compound at zero pressure. The lowest and highest regions of the phonon dispersion curves are quite dispersive in nature. The optical modes which are less dispersive are both Raman and IR active. This can be attributed to the strong intramolecular vibration arising from the most intense force constant. The acoustic modes are linear near the zone center as per their character. The flat modes present in PDC display intense peaks in phonon density of states (PHDOS). There exist three to four gaps in the optical region. However, an increase in the wavenumber of optical phonon modes is observed with increasing pressure. The partial phonon density of states (PPDOS) presented in Fig. 3.6(a) depict the contributions from hydrogen atoms in the highest optical modes, while the middle optical branches are mainly due to the vibration of both oxygen and hydrogen atoms. The contribution of the cobalt atom is mainly in the acoustic region. Further, the phonon dispersion curves at 35 GPa show the imaginary wavenumber of acoustic phonon mode which indicates dynamical instability of 2H-HCoO₂ above 35 GPa pressure (see Fig. 3.6(b)). It can also be seen from the Fig. 3.6(b) that the lower E_{1u} mode decreases with pressure and the acoustic mode of this symmetry turns imaginary along Γ -K direction. Additionally, we analysed the phonon mode patterns, particularly the symmetry properties along with the high symmetry directions of the Brillouin zone (BZ) similar to the methodology adopted from Ref. [38, 39].

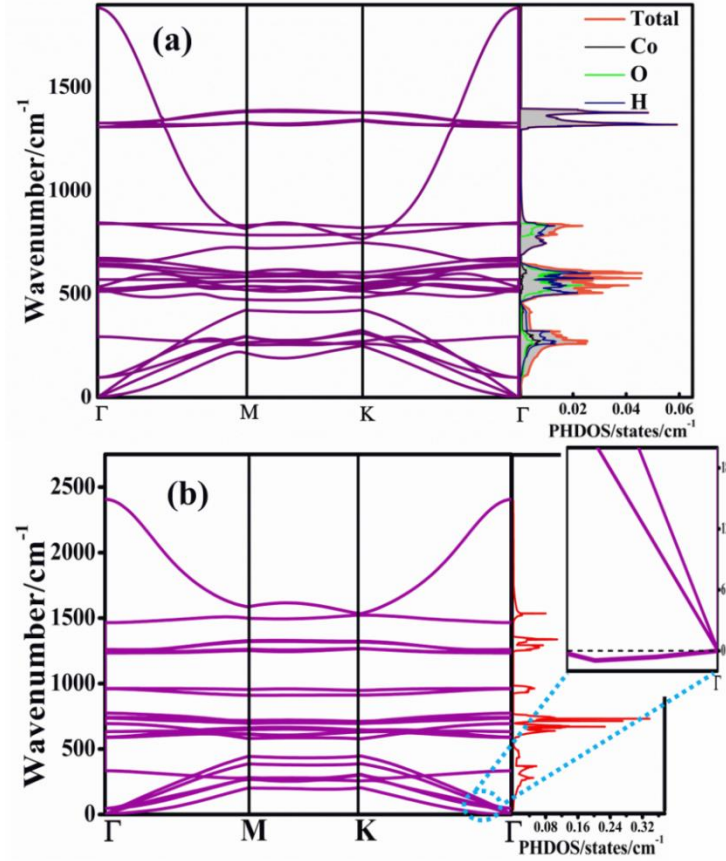


Figure 3.6: Phonon dispersion curves and phonon density of states of 2H-HCoO₂ at (a) 0 GPa and (b) 35 GPa. Inset shows the imaginary wavenumber of 2H-HCoO₂ at 35 GPa between Γ -K.

The group theory analysis yields the following decompositions for 2H phase other than zone centre (Γ) point

$$M = 6B_{1u} + 7A_{2u} + 3A_{1g} + 3B_{2u} + 5B_{1g} \quad (3.3)$$

$$\Gamma K = 11A'' + 13A' \quad (3.4)$$

In the 2H phase, the D_{6h} point group symmetry is observed at zone centre and reduces to C_{2v} at M point and C_s at K point in the BZ. It is observed that along the Γ to K direction the A_{1g} and A_{2u} modes alter to A' while E_g and E_u modes transformed into $A' + A''$ symmetry (Equation. (3.4)). The ambient and high-pressure PDCs for 3R-HCoO₂ are presented in Fig.3.7(a-b). It can be observed from the Fig. 3.7(b) that high-pressure phonon dispersion curves of the 3R phase show the dynamical instability at 40 GPa.

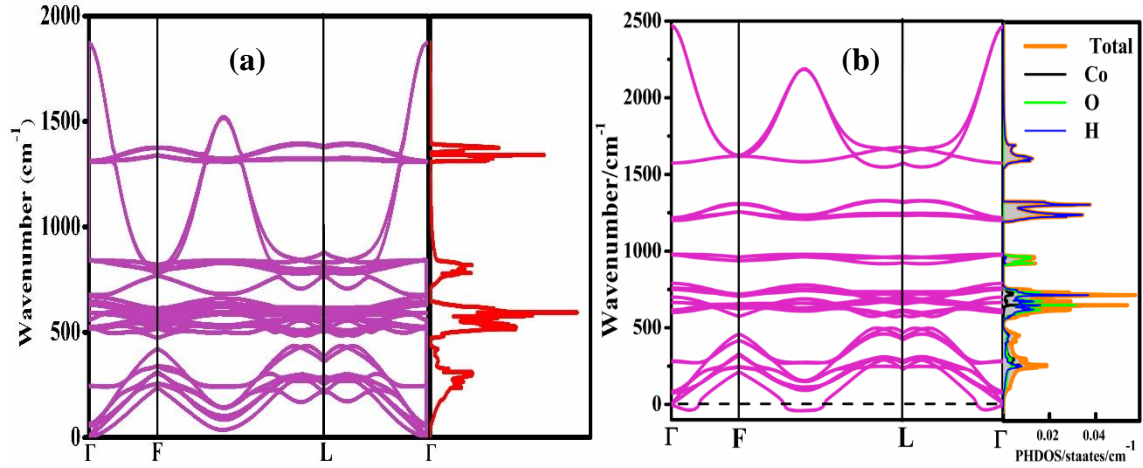


Figure 3.7: Phonon dispersion curves and phonon density of states of 3R-HCoO₂ at (a) 0 and (b) 40 GPa.

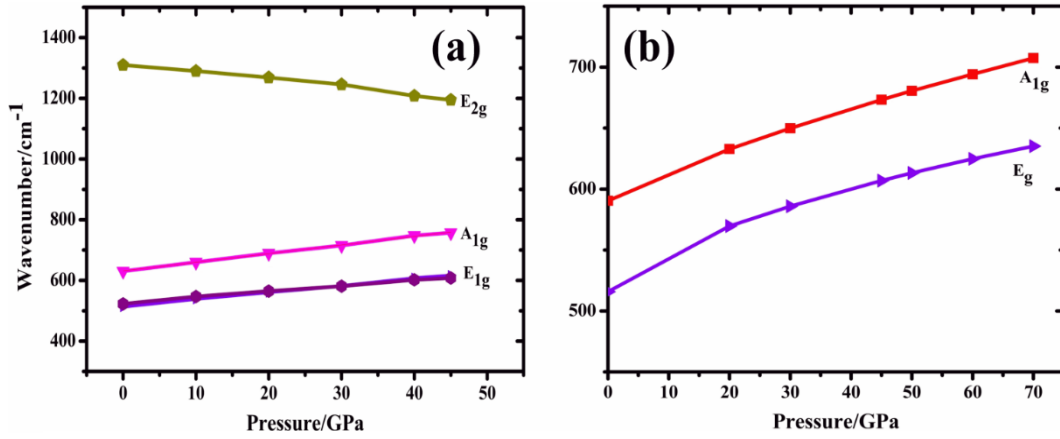


Figure 3.8: Pressure-dependent Raman active modes of (a) 2H-HCoO₂ and (b) 3R-HCoO₂.

Conventional delafossites such as CuGaO₂ and CuAlO₂ also revealed the dynamical instability due to the softening of E_{1u} mode at phase transition pressure [38, 39]. The symmetry analysis of phonon branches in the 3R phase gives the following decompositions of symmetry:

$$F = 17A + 19B \quad (3.5)$$

$$\Gamma L = 24A' + 12A'' \quad (3.6)$$

The 3R-HCoO₂ belongs to the D_{3d} point group symmetry at the zone center. Further, the symmetry reduces to C₂ and C_s at F and L points respectively. The pressure versus Raman active modes for 2H- and 3R- HCoO₂ are presented in Fig. 3.8 (a) and (b) respectively. The

wavenumbers of the Raman active modes have been fitted to second-order polynomial equation [38, 39]. The Raman active modes E_g located at 513 cm⁻¹ (see Fig. 3.8 (a)) are degenerate throughout the studied pressure range and increase linearly with pressure dependence $\omega = (513 \pm 1.94) + (2.19 \pm 0.20)P - (0.006 \pm 0.004)P^2$. The A_{1g} mode located at 610 cm⁻¹ shows the linearly increasing behaviour with pressure dependence $\omega = (610.46 \pm 1.98) + (2.98 \pm 0.21)P - (0.003 \pm 0.004)P^2$ where ω is expressed in cm⁻¹ and P in GPa. The dependence of the Raman active E_{2g} mode is also linear and its pressure dependence is given by $\omega = (1309 \pm 2) - 1.51 \pm 0.26)P - (0.0232 \pm 0.0055)P^2$. In the 2H phase, the E_g and A_{1g} modes show the increasing behaviour, while the E_{2g} mode decreases with increasing pressure. The pressure coefficient of E_g and A_{1g} mode is positive while it is negative for the E_{2g} mode. In the case of 3R-HCoO₂ only two modes are Raman active namely E_g located at 515 cm⁻¹ and A_{1g} at 590 cm⁻¹. As pressure increases, the E_g and A_{1g} modes show the linear increment in wavenumbers. The E_g mode shows the pressure dependence $\omega = (515.59 \pm 2.67) + (2.70 \pm 0.16)P - (0.015 \pm 0.002)P^2$ while A_{1g} mode shows the pressure dependency $\omega = (590.97 \pm 0.87) + (2.18 \pm 0.05)P - (0.00753 \pm 0.00007)P^2$ similar to the other delafossites [41].

B. Raman spectra

The calculated Raman spectra of 2H- and 3R-HCoO₂ are presented in Fig. 3.9 (a) and (b) respectively. The Raman spectra of 2H-HCoO₂ show three Raman active modes: 1A_{1g}+2E_g, whereas in the case of 3R-HCoO₂, there are only two Raman active modes namely A_{1g} and E_g which are confirmed from the group theory analysis. The Raman spectra show good agreement with the available experimental Raman results [13, 42, 43]. In the Raman spectra of 2H-HCoO₂, the peaks located at 513, 610, and 1307 cm⁻¹ are assigned to E_g, A_{1g}, and E_{2g} modes respectively while in the case of 3R-HCoO₂, peaks at 515 and 590 cm⁻¹ are associated to E_g

and A_{1g} modes. Both Raman spectra are similar except for one additional peak at 1307 cm⁻¹ in the case of 2H-HCoO₂.

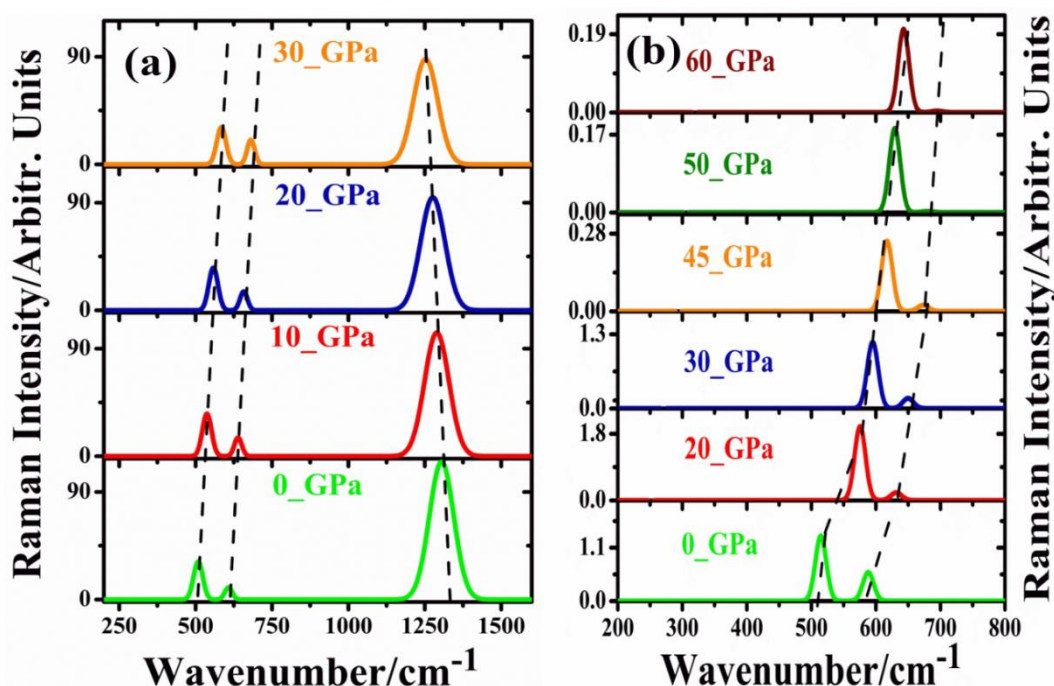


Figure 3.9: Calculated Raman spectrum of (a) 2H-HCoO₂ and (b) 3R-HCoO₂ at different pressures.

The E_g mode arises due to Co-O bending vibrations in the perpendicular direction of O-Co-O bonds while A_{1g} mode is associated to the Co-O stretching vibrations parallel to the c-axis. The 1307 cm⁻¹ mode in 2H-HCoO₂ arises due to the O-H vibrations which is absent in 3R-HCoO₂. The wavenumber of Raman modes along with available experimental data are summarized in Table 3.2. A good agreement with experimental data for E_g as well as A_{1g} modes of 2H and 3R phases is observed, while a slight overestimation of E_{2g} mode is observed for 2H phase. The pressure dependent Raman spectra of 2H-HCoO₂ show that the intensity of E_g mode remains constant, while the intensity of A_{1g} mode increases with pressure. Both E_g and A_{1g} modes undertake blue shift and redshift with pressure. A peak broadening is observed for E_{2g} mode with the increase in pressure. However, the pressure dependent Raman spectra of the 3R phase show a significant blue shift in both E_g and A_{1g} modes with increasing pressure. The intensity of E_g mode increases whereas the intensity of A_{1g} mode decreases with pressure. The

A_{1g} mode in 3R-HCoO₂ which appears up-to 45 GPa almost disappears beyond this pressure. The softening of A_{1g} mode in 3R-HCoO₂ is the consequence of phase transition in 3R-HCoO₂. Previous pressure dependent Raman spectroscopic studies of 3R delafossite show the softening of A_{1g} mode at phase transition pressure [38, 39, 44]. The A_{1g} mode is related to the O-Co-O stretching vibration parallel to the c-axis and as we see from Fig 3.3(b), the c-axis shows a more compressible nature as compared to the a-axis.

Table 3.2: Calculated Raman Modes of 2H- and 3R- HCoO₂ along with experimental (Exp.) data.

Raman modes	3R (cm ⁻¹)	Exp. (cm ⁻¹)	2H (cm ⁻¹)	Exp. (cm ⁻¹)
E_g	515	504 ^[13] , 503 ^[42]	513	504 ^[13]
A_{1g}	590	635 ^[41] , 635 ^[13] , 640 ^[13] , 1145 ^[13] , 642 ^[13]	610	635 ^[13]
E_{2g}	-	-	1307	1220 ^[13]

3.4 Elastic Properties

To investigate the mechanical stability of 2H- and 3R-HCoO₂, we have calculated the elastic constants. There are five independent elastic constants i.e. C₁₁, C₁₂, C₁₃, C₃₃, and C₄₄ for both phases. The mechanical stability of any compound depends on the positive stiffness matrix and Born stability criteria given as [45-46]:

$$C_{44} > 0, \quad C_{11} > |C_{12}|, \quad C_{33}(C_{11} + C_{12}) > 2C_{13}^2 \quad (3.7)$$

Calculated pressure dependent elastic constants, bulk modulus, shear modulus, and Young's modulus are summarized in Table 3.3 and 3.4 for 2H- and 3R HCoO₂ respectively. For the accurate analysis of pressure-dependent mechanical properties, we investigated the variation of elastic constants, and different elastic moduli and are presented them in Fig. 3.10 (a-c) and Fig. 3.11 (a-b).

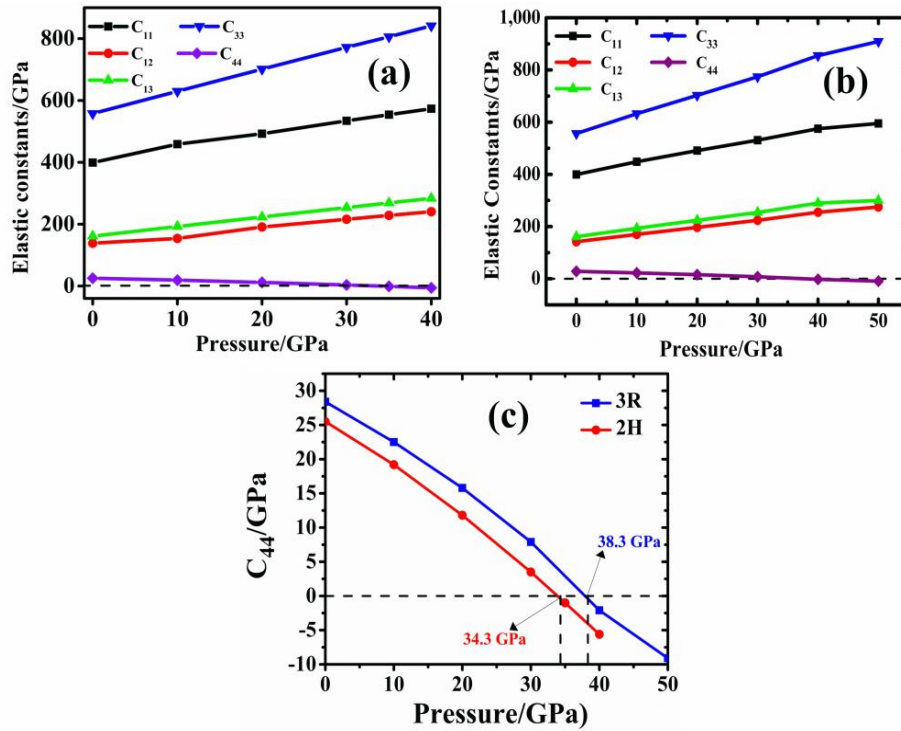


Figure 3.10: Calculated elastic constants of (a) 2H-HCoO₂ and (b) 3R-HCoO₂ at different pressures. (c) Pressure-dependent C₄₄ elastic mode of 2H- and 3R-HCoO₂.

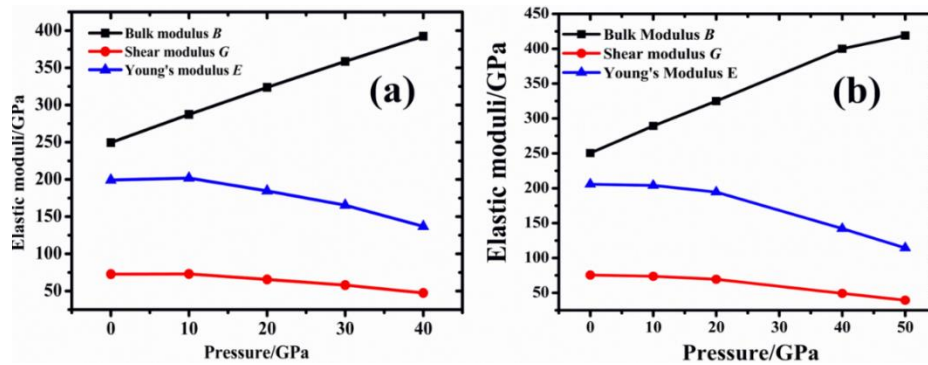


Figure 3.11: Elastic moduli, bulk (B), shear (G), and Young's (E) modulus as a function of pressure for (a) 2H- for peer review HCoO₂ and (b) 3R-HCoO₂.

Table 3.3, 3.4, and Fig. 3.10 depict that the Born stability criteria of mechanical stability are satisfied for 2H and 3R-HCoO₂ below 34.3 GPa and 38.3 GPa respectively. Further, C₄₄ becomes imaginary beyond 34.3 and 38.3 GPa for 2H and 3R-HCoO₂ respectively. Calculated elastic constants (C₁₁, C₁₂, C₁₃, and C₃₃) show the linear increment with pressure, however, the C₄₄ mode shows the decrement with pressure. Also, it can be seen from Fig. 3.11 (a-c) that the bulk modulus (B) increases with pressure while shear modulus (G) and Young modulus (E) decreases.

Table 3.3: Pressure dependent elastic constants, bulk (B), shear (G) and Young's (E) modulus as well as B/G ratio and Poisson's ratio of 2H- HCoO₂.

Elastic Constants (GPa)	0 GPa	10 GPa	20 GPa	30 GPa	35 GPa	40 GPa
C ₁₁	399.4	458.8	492.5	534.2	554.3	573.5
C ₁₂	138.7	154.1	190.9	216.0	228.3	240.4
C ₁₃	161.4	192.6	223.5	253.7	268.7	283.7
C ₃₃	555.7	629.7	701.6	771.9	806.6	841.2
C ₄₄	25.5	19.2	11.8	3.5	-1.0	-5.6
B (GPa)	249.5	287.3	323.7	358.6	375.7	392.5
G (GPa)	72.8	73.0	65.6	58.0	53.2	47.4
E (GPa)	199.2	201.9	184.5	165.3	152.4	136.9
B/G	3.42	3.93	4.93	6.18	7.06	8.28
Poisson ratio	0.37	0.38	0.40	0.42	0.43	0.44

Table 3.4: Pressure dependent elastic constants, bulk (B), shear (G) and Young's (E) modulus as well as B/G ratio and Poisson's ratio of 3R- HCoO₂.

Elastic Constants (GPa)	0 GPa	10 GPa	20 GPa	30 GPa	40 GPa
C ₁₁	399.7	448.4	491	531	575
C ₁₂	141.9	170.0	197	224	235
C ₁₃	161.2	193.4	224	254	290
C ₃₃	556.5	632.5	703	774.4	855
C ₄₄	28.4	22.5	15.8	7.9	-2.1
B (GPa)	250.43	289.35	325	360	400
G (GPa)	75.47	73.7	69.4	62.11	49.3
E (GPa)	205.73	203.99	194.5	176.22	142.0
B/G	3.31	3.93	4.68	5.79	8.11
Poisson ratio	0.36	0.38	0.40	0.42	0.44

It is observed that the bulk modulus is greater than the shear modulus ($B > G$) which indicates that the shear modulus limits the stability of this compound [47]. It can also be observed that the B/G ratio is greater than 1.75 which shows the ductile nature of HCoO₂ according to Pugh's criteria [48].

3.5 Conclusions

In summary, the pressure dependent structural, electronic, vibrational, and elastic properties of 2H- and 3R-HCoO₂ are investigated within the framework of density functional theory. Our calculated results show a reasonable agreement with available experimental data. An accurate description of the electronic band structure and band gap of the HCoO₂ is obtained by employing the Hubbard U parameter. Calculated Raman spectra determine two Raman active modes i.e. E_g (Co-O bending) and A_{1g} (Co-O stretching) in 2H- and 3R- HCoO₂, while an additional E_{2g} mode (O-H bending) is observed only in the 2H phase. The peak broadening nature of E_{2g} mode is observed with pressure which indicates the decrement in O-H bonding. The phonon dispersion curves (PDCs) show dynamical instability for both 2H and 3R phases of HCoO₂ at 35 GPa and 40 GPa induced by the softening of E_{2u} and A_{2u} mode. The pressure dependency of phonon modes shows linear variation. The 2H and 3R-HCoO₂ are mechanically stable up to 34.3 and 38.3 GPa respectively. The elastic constant C₄₄ turns negative after these pressures indicating violation of the Born stability criteria. We find a clear link between shear modulus and phonon modes suggesting a shear modulus driven dynamical instability in both phases of HCoO₂.

References

1. A. N. Banarjee, K. K. Chattopadhyay, Nova Science Publishers Inc, United States 2009.
2. X. Li, J. Wang, J. Zhang, Y. Li, Z. Hu, J. Chu, *RSC Adv.* **6**, 27136 (2016).
3. I. Sinnarasa, Y. Thimont, L. Presmanes, A. Barnabe, P. Tailhades, *Nanomaterials.* **7**, 157 (2017).
4. T. Pauporte, L. Mendoza, M. Cassir, M. C. Bernard, J. Chivot, *J. Electrochem. Soc.* **152**, 49 (2005).
5. K. K. Lee, P. Y. Loh, C. H. Sow, W. S. Chin, *Biosens. Bioelectron.* **39**, 255 (2013).
6. Y. Chen, J. Zhou, P. Maguire, R. O'Connell, W. Schmitt, Y. Li, H. Zhang, *Sci. rep.* **6**, 20704 (2016).

7. P. L. S. G. Poizot, S. Laruelle, S. Grugeon, L. Dupont, J. M. Tarascon, *Nature*. **407**, 496 (2000).
8. H. Kawazoe, M. Yasukawa, H. Hyodo, M. Kurita, H. Yanagi, H. Hosono, *Nature*. **389**, 939 (1997).
9. C. Ruttanapun, *J. App. Phys.* **114**, 113108 (2013).
10. M. N. Huda, Y. Yan, A. Walsh, S. H. Wei, M. M. Al-Jassim, *Phys. Rev. B*. **80**, 035205 (2009).
11. T. Jiang, B. Polteau, Y. Farré, L. Cario, C. Latouche, Y. Pellegrin, S. Jobic, *Ino. chem.* **56**, 7922 (2017).
12. T. F. Cerqueira, S. Lin, M. Amsler, S. Goedecker, S. Botti, M. A. Marques, *Chem. of Mat.* **27**, 4562 (2015).
13. C. Burlet, H. Goethals, Y. Vanbrabant, *Spectrochim Acta A Mol. Biomol. Spectrosc.* **159**, 90 (2016).
14. S. R. Alvarado, Y. Guo, T. P. A. Ruberu, A. Bakac, J. Vela, *J. Phys. Chem. C*. **116**, 10382 (2012).
15. M. Deliens, H. Goethals, *Mineral Mag.* **39**, 152 (1973).
16. J. Chen, A. Selloni, *J. Phys. Chem. C*. **117**, 20002 (2013).
17. S. He, Y. Huang, J. Huang, W. Liu, T. Yao, S. Jiang, Q. Liu, *J. Phys. Chem. C*. **119**, 26362 (2015).
18. P. Hohenberg, W. Kohn, *Phys. Rev. B*. **136**, 864 (1964).
19. P. Giannozzi, S. Baroni, N. Bonini, M. Calandra, R. Car *et al.*, *J. Phys. Condens. Matter.* **21**, 395502 (2009).
20. J. P. Perdew, K. Burke, M. Ernzerhof, *Phys. Rev. Lett.* **77**, 3865 (1996).
21. J. P. Perdew, A. Zunger, *Phys. Rev. B*. **23**, 5048 (1981).
22. V. I. Anisimov, F. Aryasetiawan, A. I. Lichtenstein, *J. Phys. Condens. Matter.* **9**, 767 (1997).
23. J. D. Pack, H. J. Monkhorst, *Phys. Rev. B*. **16**, 1748 (1977).
24. R. M. Wentzcovitch, J. L. Martins, G. D. Price, *Phys. Rev. Lett.* **70**, 3947 (1993).
25. J. D. Head, M. C. Zerner, *Chem. Phys. Lett.* **122**, 264 (1985).
26. S. D. Gupta, P. K. Jha, *Earth and Plant. Sci. Lett.* **401**, 31 (2014).
27. S. D. Gupta, S. K. Gupta, P. K. Jha, N. N. Ovsyuk, *J. Raman Spectrosc.* **44**, 926 (2013).
28. S. Baroni, S. de Gironcoli, A. Dal Corso, P. Giannozzi, *Rev. Mod. Phys.* **73**, 515 (2001).
29. N. E. Christensen, A. Svane, R. Laskowski, B. Palanivel, P. Modak, A. N. Chantis, M. van Schilfhaarde, T. Kotani, *Phys. Rev. B*. **81**, 045203 (2010).

30. S. Gilliland, J. Pellicer-Porres, A. Segura, A. Muñoz, P. Rodríguez-Hernández, D. Kim, M. S. Lee, T. Y. Kim, *Phys. Status. Solidi B.* **244**, 309 (2007).
31. Wen-Ting Liu, Qi-Jun Liu, Zheng-Tang Liu, *Physica. B.* **407**, 4665 (2012).
32. H. Zhu, T. Cai, M. Que, J-P. Song, B. M. Rubenstein, Z. Wang, O. Chen, *J. Phys. Chem. Lett.* **9**, 4199 (2018).
33. E. Kroumova, M. I. Aroyo, A. Kirov, C. Capillas, S. Ivantchev, H. Wondratschek, M. I. Aroyo, A. Kirov, C. Capillas, *Phase. Transit.* **76**, 155 (2010).
34. S. Kumar, H. C. Gupta, *Comput. Theor. Chem.* **977**, 78 (2011).
35. A. B. Garg, R. Rao, *Crystals* **8**, 255 (2018).
36. P. K. Jha, S. P. Sanyal, *Physica. C.* **261**, 259 (1996).
37. P. K. Jha, *Phys. Rev. B.* **72**, 214502 (2005).
38. J. Pellicer-Porres, A. Segura, E. Martínez, A. M. Saitta, A. Polian, J. C. Chervin, B. Canny, *Phys. Rev. B.* **72**, 064301(2005).
39. J. Pellicer-Porres, D. Martinez-Garcia, A. Segura, P. Rodriguez-Hernandez, A. Munoz, J. C. Chervin, D. Kim, *Phys. Rev. B.* **74**, 184301(2006).
40. D. Upadhyay, A. Patel, A. Pratap, P. K. Jha, *AIP Conf. Proc.* **1942**, 090027 (2018).
41. N. P. Salke, K. Kamali, T. R. Ravindran, G. Balakrishnan, R. Rao, *Vib. Spectrosc.* **81**, 112 (2015).
42. J. Yang, H. Liu, W. N. Martens, R. L. Frost, *J. Phys. Chem. C.* **114**, 111 (2009).
43. C. W. Tang, C. B. Wang, S. H. Chien, *Thermochim. Acta.* **473**, 68 (2008).
44. N. P. Salke, A. B. Garg, R. Rao, S. N. Achary, M. K. Gupta, R. Mittal, A. K. Tyagi, *J. App. Phys.* **115**, 133507 (2014).
45. Q. J. Liu, Z. T. Liu, L. P. Feng, *Physica B.* **405**, 2028 (2010).
46. G. V. Sin'Ko, N. A. Smirnov, *J. Phys. Condens. Matter.* **14**, 6989 (2002).
47. I. R. Shein, A. L. Ivanovskii, *J. Phys. Condens. Matter.* **20**, 415218 (2008).
48. S. F. Pugh, *Philos. Mag.* **45**, 823 (1954).